Transport and deposition of dilute microparticles in turbulent thermal convection

Ao Xu,[1, a)] Shi Tao,[2] Le Shi,[3] and Heng-Dong Xi[1]

[1)]*School of Aeronautics, Northwestern Polytechnical University, Xi'an 710072, China*

[2)]*Key Laboratory of Distributed Energy Systems of Guangdong Province, Dongguan University of Technology, Dongguan 523808, China*

[3)]*State Key Laboratory of Electrical Insulation and Power Equipment, Center of Nanomaterials for Renewable Energy, School of Electrical Engineering, Xi'an Jiaotong University, Xi'an 710049, China*

(Dated: 14 July 2020)

We analyze the transport and deposition behavior of dilute microparticles in turbulent Rayleigh-Bénard convection. Two-dimensional direct numerical simulations were carried out for the Rayleigh number (Ra) of 10^8 and the Prandtl number (Pr) of 0.71 (corresponding to the working fluids of air). The Lagrangian point particle model was used to describe the motion of microparticles in the turbulence. Our results show that the suspended particles are homogeneously distributed in the turbulence for Stokes number (St) less than 10^{-3}, and they tend to cluster into bands for $10^{-3} \lesssim St \lesssim 10^{-2}$. At even larger St, the microparticles will quickly sediment in the convection. We also calculate the mean-square displacement (MSD) of the particle's trajectories. At short time intervals, the MSD exhibits a ballistic regime, and it is isotropic in vertical and lateral directions; at longer time intervals, the MSD reflects a confined motion for the particles, and it is anisotropic in different directions. We further obtained a phase diagram of the particle deposition positions on the wall, and three deposition states depending on the particle's density and diameter were identified. An interesting finding is that the dispersed particles preferred to deposit on the vertical wall where the hot plumes arise, which is verified by tilting the cell and altering the rotation direction of the large-scale circulation. [a]

[a)] The following article has been submitted to Physics of Fluids. After it is published, it will be found at Link (https://publishing.aip.org/resources/librarians/products/journals/).

[a)]Electronic mail: axu@nwpu.edu.cn

I. INTRODUCTION

Transport and deposition of solid particles (or liquid droplets) in turbulent thermal convection occur ubiquitously in environmental science[1–4]. For example, suspended atmospheric pollutant particles (PM10, PM2.5) that originated from dust and smoke will severely influence the air quality[5,6]. Another example is that pathogen laden droplets in confined indoors, which will cause viral and bacterial infectious diseases (SARS, COVID-19) spreading in hospitals, schools, and airplanes[7–10]. In such dispersed multiphase flow, the evolution of the phase interface may not be a primary concern[11]. From the aspect of particle kinematics, important control parameters include the density ratio of the particle to its surrounding fluid $\Gamma = \rho_p/\rho_f$, and the size ratio $\Xi = d_p/l_f$. Here, ρ_p and d_p are the particle density and particle size, respectively. ρ_f is the fluid density, l_f is the characteristic fluid length. When $\Xi \ll 1$, the Lagrangian particle model can be used to track the dispersed phase. Moreover, when the volume fraction of the dispersed phase is small, the dominant effect is that of the carrier flow on the dynamics of the dispersed phase, but not *vice versa*. Thus, a one-way interphase coupling approach can be adopted to track the motions of particles[12,13]. Previous studies have shown that even in homogeneous isotropic turbulence, dispersed particles may not distribute homogeneously but exhibit preferential concentration[14–17]. For light particles with a density ratio of $\Gamma \ll 1$, they concentrate in regions of high vorticity; for heavy particles with a density ratio of $\Gamma \gg 1$, they are expelled from rotating regions.

Due to the injected buoyancy and the effect of the domain boundaries, turbulent thermal convection is generally inhomogeneous and anisotropic. A simple paradigm system to study thermal convection is the Rayleigh-Bénard (RB) cell, where a fluid layer is heated from the bottom and cooled from the top[18–24]. The control parameters of the RB system include the Rayleigh number $Ra = \beta g \Delta_T H^3/(\nu_f \kappa_f)$ and the Prandtl number $Pr = \nu_f/\kappa_f$. The Ra describes the strength of buoyancy relative to thermal and viscous dissipative effects. The Pr describes thermophysical fluid properties. Here, β, κ_f, and ν_f are the thermal expansion coefficient, thermal diffusivity, and kinematic viscosity of the fluid, respectively. g is the gravitational acceleration. Δ_T is the imposed temperature difference between the top and bottom fluid layers of height H. In the RB convection, ubiquitous coherent structures include thermal plumes and large-scale circulation (LSC)[25,26]. Specifically, sheet-like plumes that detached from boundary layers transform into mushroom-like ones via mixing, merging, and clustering[27]. Due to plume-vortex and plume-plume interactions, thermal plumes further self-organize into the LSC that spans the size of the convection cell[28].

Although the dynamics of single-phase turbulent thermal convection has been thoroughly investigated, the complex interactions between dispersed immiscible phase and its surrounding fluid in turbulent thermal convection remain less explored. One of the few studies by Puragliesi et al.[29] focused on particle deposition in side-heated convection cell (i.e., heated from one vertical side and cooled from the other vertical side). They found that a strong recirculating zone contributes to the decreased gravitational settling, thus resulting in particles suspending with longer time. Because the driven force, namely the temperature gradient, in side-heated convection cell is perpendicular to that in the RB convection cell, the fluid and particle dynamics are expected to be different in these two cells. Lappa[30] analyzed the pattern produced by inertial particles dispersed in the localized rising thermal plume. He identified the average behavior of particles by revealing the mean evolution. It should be noted that although thermal plumes are the building blocks of turbulent thermal convection, the LSC, which is another essential feature of the turbulent thermal convection, is missing in such analysis. In addition to the one-way coupling between the dispersed phase and the carrier flow, Park et al.[31] further investigated the RB turbulence modified by inertial and thermal particles. Changes of integrated turbulent kinetic energy and heat transfer efficiency were quantified. Results showed that particles with Stokes number (to be defined in Sec. II C) of order unity maximize the heat transfer efficiency. However, particles with such high Stokes number (either heavy density or large size) will sediment quickly in the air, which may be of limited interest for studying suspended atmospheric pollutant particles or pathogen laden droplets.

In this work, our objective is to shed light on the dynamics of atmospheric pollutant particles or pathogen laden droplets. We simulate transport and deposition of dilute microparticles in an RB convection cell with air as the working fluid (i.e., $Pr = 0.71$) at high Ra number (i.e., $Ra = 10^8$), such that ubiquitous features of the turbulent thermal convection (including thermal plumes and the LSC) naturally arise. We choose the typical particle parameters as $10\ \mu\text{m} \leq d_p \leq 100\ \mu\text{m}$ and $400\ \text{kg/m}^3 \leq \rho_p \leq 4000\ \text{kg/m}^3$, and the corresponding particle Stokes number (i.e., $3.67 \times 10^{-4} \leq St \leq 0.37$) is much lower than that by Park et al.[31] (i.e., $0.1 < St < 15$). The rest of this paper is organized as follows: In Sec. II, we present numerical details for the simulations, including direct numerical simulation of thermal turbulence and Lagrangian point particle model. In Sec. III, we analyzed the particle transport behavior via flow visualization and particle mean-square displacement calculation; followed by statistics of particle deposition behavior, such as time history of the particle deposition ratio and phase diagram of particle deposition location. In Sec. IV, the main findings of the present work are summarized.

II. NUMERICAL METHOD

A. Numerical model for incompressible thermal flows

In incompressible thermal flows, temperature variation will cause density variation, thus resulting in a buoyancy effect. Following the Boussinesq approximation, the temperature can be treated as an active scalar, and its influence on the velocity field is realized through the buoyancy term. The governing equations can be written as

$$\nabla \cdot \mathbf{u}_f = 0 \tag{1a}$$

$$\frac{\partial \mathbf{u}_f}{\partial t} + \mathbf{u}_f \cdot \nabla \mathbf{u}_f = -\frac{1}{\rho_0}\nabla p + \nu_f \nabla^2 \mathbf{u}_f + g\beta(T - T_0)\hat{\mathbf{y}} \tag{1b}$$

$$\frac{\partial T}{\partial t} + \mathbf{u}_f \cdot \nabla T = \kappa \nabla^2 T \tag{1c}$$

where $\mathbf{u}_f$, p and T are the fluid velocity, pressure and temperature, respectively. ρ_0 and T_0 are the reference density and temperature, respectively. $\hat{\mathbf{y}}$ is the unit vector in the vertical direction. In the above equations, all the transport coefficients are assumed to be constants.

We adopt the lattice Boltzmann (LB) method[32–35] as the numerical tool for direct numerical simulation of turbulent thermal convection. The advantages of the LB method include easy implementation and parallelization, as well as low numerical dissipation[36]. In the LB method, to solve Eqs. 1a and 1b, the evolution equation of the density distribution function is written as[32,33]

$$f_i(\mathbf{x} + \mathbf{e}_i\delta_t, t + \delta_t) - f_i(\mathbf{x}, t) = -(\mathbf{M}^{-1}\mathbf{S})_{ij}\left[\mathbf{m}_j(\mathbf{x}, t) - \mathbf{m}_j^{(\mathrm{eq})}(\mathbf{x}, t)\right] + \delta_t F_i' \tag{2}$$

To solve Eq. 1c, the evolution equation of temperature distribution function is written as[32,33]

$$g_i(\mathbf{x} + \mathbf{e}_i\delta_t, t + \delta_t) - g_i(\mathbf{x}, t) = -(\mathbf{N}^{-1}\mathbf{Q})_{ij}\left[\mathbf{n}_j(\mathbf{x}, t) - \mathbf{n}_j^{(\mathrm{eq})}(\mathbf{x}, t)\right] \tag{3}$$

Here, f_i and g_i are the density and temperature distribution function, respectively. $\mathbf{x}$ is the fluid parcel position, t is the time, and δ_t is the time step. $\mathbf{e}_i$ is the discrete velocity along the ith direction. $\mathbf{M}$ is a 9×9 orthogonal transformation matrix based on the D2Q9 discrete velocity model; $\mathbf{N}$ is a 5×5 orthogonal transformation matrix based on the D2Q5 discrete velocity model. The equilibrium moments $\mathbf{m}^{(\mathrm{eq})}$ in Eq. 2 are

$$\mathbf{m}^{(\mathrm{eq})} = \rho\left[1,\ -2 + 3|\mathbf{u}_f|^2,\ 1 - 3|\mathbf{u}_f|^2,\ u_f,\ -u_f,\ v_f,\ -v_f,\ 2u_f^2 - v_f^2,\ u_f v_f\right]^T \tag{4}$$

The equilibrium moments $\mathbf{n}^{(\mathrm{eq})}$ in Eq. 3 are

$$\mathbf{n}^{(\mathrm{eq})} = \left[T,\ u_f T,\ v_f T,\ a_T T, 0\right]^T \tag{5}$$

a_T is a constant determined by thermal diffusivity as $a_T = 20\sqrt{3}\kappa - 6$. The relaxation matrix $\mathbf{S}$ is $\mathbf{S} = \mathrm{diag}(s_\rho, s_e, s_\varepsilon, s_j, s_q, s_j, s_q, s_\nu, s_\nu)$, and the kinematic viscosity of the fluid is calculated as $\nu = c_s^2(\tau_f - 0.5)$. The relaxation matrix $\mathbf{Q}$ is $\mathbf{Q} = \mathrm{diag}(0, q_\kappa, q_\kappa, q_e, q_\nu)$, where $q_\kappa = 3 - \sqrt{3}$, $q_e = q_\nu = 4\sqrt{3} - 6$.

The macroscopic fluid variables of density ρ, velocity $\mathbf{u}_f$ and temperature T are calculated as $\rho = \sum_{i=0}^{8} f_i$, $\mathbf{u} = \left(\sum_{i=0}^{8} \mathbf{e}_i f_i + \mathbf{F}/2\right)/\rho$, and $T = \sum_{i=0}^{4} g_i$, respectively. More numerical details on the LB method and validation of the in-house code can be found in our previous work[37–39].

B. Kinematic equation for the particles

We consider small particles such that their presences do not modify the turbulence structure, namely one-way coupling between the multiphase. Here, 'small' means the diameter of the particle is smaller than the Kolmogorov length scale of the turbulence; however, the diameter of the particle should still be much larger than the molecular mean free path, such that the effect of Brownian motion can be neglected. In addition, the particles are assumed to be isotropic, such that we only consider the motion of the particle and neglect the rotation of the particle[40,41]. Specifically, the particles' motions are described by Newton's second law as

$$m_p \frac{d\mathbf{u}_p(t)}{dt} = \mathbf{F}_{\text{total}}(t) = \mathbf{F}_G(t) + \mathbf{F}_D(t) \tag{6}$$

The total force $\mathbf{F}_{\text{total}}$ exerted on the particle include the net gravitational force $\mathbf{F}_G$ and the drag force $\mathbf{F}_D$. Specifically, particles experience a gravitational force in the direction of gravitational acceleration, as well as buoyancy in the opposite direction. The net gravitational force $\mathbf{F}_G$ is given by

$$\mathbf{F}_G = \rho_p V_p \mathbf{g} - \rho_f V_p \mathbf{g} \tag{7}$$

where ρ_p and V_p are the density and volume of the particle, respectively. Meanwhile, the particle experiences a drag force that acts to catch up with the changing velocity of the surrounding fluid. The drag force $\mathbf{F}_D$ is given by

$$\mathbf{F}_D = \frac{m_p}{\tau_p}\left(\mathbf{u}_f - \mathbf{u}_p\right) f(Re_p) \tag{8}$$

where m_p and $\mathbf{u}_p$ are the mass and velocity of the particle, respectively. $\tau_p = \rho_p d_p^2/(18\mu_f)$ is the particle response time and d_p is the particle diameter. The particle Reynolds number $Re_p = d_p|\mathbf{u}_f - \mathbf{u}_p|/\nu_f$ determines the coefficient $f(Re_p)$. When Re_p is much less one, namely a Stokes drag law is valid, we have $f(Re_p) \approx 1$. In general, Clift et al.[42] give the relationship $f(Re_p) = 1 + 0.15Re_p^{0.687}$ for $Re_p < 40$.

C. Simulation settings

We consider the particle motions in a 2D convection cell with size $H \times H$. The top and bottom walls of the cell are kept at a constant cold and hot temperatures, respectively; the other two vertical walls are adiabatic. All four walls impose no-slip velocity boundary conditions. Our simulation protocol is as follows. We start the simulation of single-phase turbulent thermal convection, namely without considering the particles' motion. The particles are released in the turbulence after statistically stationary state has reached, which takes 500 t_f. Here, $t_f = \sqrt{H/(g\beta\Delta_T)}$ denotes free-fall time units. We then advance the fluid flows and the motion of the particles simultaneously. A total number of 10,000 particles are initially placed at the cell central region (see Fig. 1 for the illustration, the 10,000 particles are initially grouped into a 100×100 array, and each particle is placed half grid spacing away from the other). The initial velocities of the particles are equal to that of the local fluid. The initial particle configuration approximates the transport of pollutant particles emitted from a source, and the dilute particles may mimic the particle-laden fluid in a cough[43]. We average 2,000 t_f to obtain statistics for the turbulent flows and the particles. When a particle hits the wall, we assume it will deposit on the wall and no longer transport in the convection cell.

We provide simulation results for a fixed Rayleigh number of $Ra = 10^8$ and Prandtl number of $Pr = 0.71$ (corresponding to the working fluids of air at 300 K). Other detailed simulation parameters are listed in Table 1. The mesh size is 513×513, such that the grid spacing Δ_g and time interval Δ_t is properly resolved to compare with the Kolmogorov and Batchelor scales. Here, the Kolmogorov length scale is estimated by the global criterion $\eta_K = \left(\nu^3/\langle \varepsilon_u \rangle_{V,t}\right)^{1/4} = HPr^{1/2}/\left[Ra(Nu-1)\right]^{1/4}$, the Batchelor length scale is estimated by $\eta_B = \eta_K Pr^{-1/2}$, and the Kolmogorov time scale is estimated as $\tau_{\eta_K} = \sqrt{\nu/\langle \varepsilon_u \rangle_{V,t}} = t_f\sqrt{Pr/(Nu-1)}$. The global heat transport is measured by the volume-averaged Nusselt number as $Nu = 1 + \sqrt{PrRa}\langle vt \rangle_{V,t}$, while the Reynolds number $Re = \sqrt{\langle u^2 + v^2 \rangle_{V,t}}H/\nu$ measures the global strength of the convection. Here, $\langle \cdots \rangle_{V,t}$ denotes the volume and time average. ε_u denotes the kinetic energy dissipation rates, and its global average can be related to the Nusselt number via[44] the exact relation $\langle \varepsilon_u \rangle_{V,t} = \nu^3 Ra(Nu-1)/(H^4 Pr^2)$. Simulation results have shown that grid spacing satisfies $\max(\Delta_g/\eta_K, \Delta_g/\eta_B) \leq$

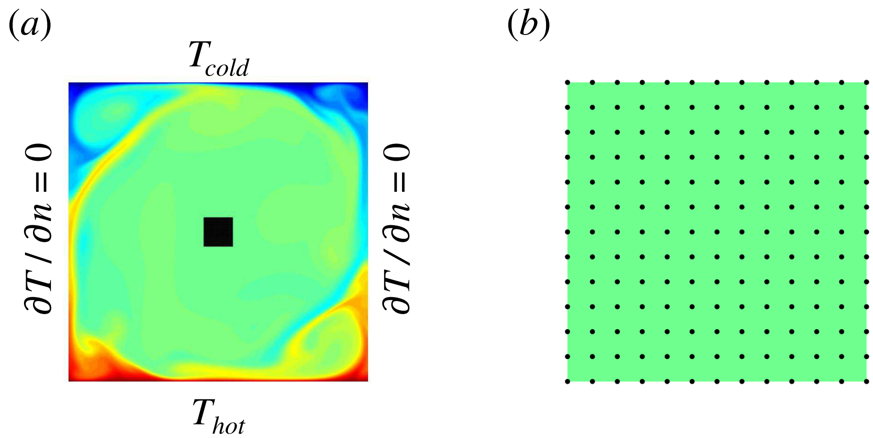

FIG. 1. (*a*) Illustration of the particles' initial positions in the convection cell, the contour represents the instantaneous temperature field; (*b*) an enlarged view of the central region in (*a*). The black dots represent the particles, whose sizes have been artificially increased for the convenience of flow visualization.

0.51, which ensures the spatial resolution; the time intervals are $\Delta_t \leq 0.0006\tau_{\eta_K}$, thus adequate temporal resolution is guaranteed. In addition, our results for Nusselt and Reynolds numbers (i.e., $Nu = 25.36$, $Re = 3602$) are consistent with previous results reported by Zhang et al.[45] (i.e., $Nu = 25.25$, $Re = 3662$).

TABLE I. Fluid properties and simulation parameters.

Parameter	Value
Rayleigh number (Ra)	10^8
Prandtl number (Pr)	0.71
Reference temperature (T_0)	300 K
Reference fluid density (ρ_0)	1.18 kg/m^3
Thermal expansion coefficient (β)	3.36×10^{-3} K^{-1}
Kinematic viscosity (ν_f)	1.58×10^{-5} m^2/s
Thermal diffusivity (κ_f)	2.21×10^{-5} m^2/s
Temperature differences (Δ_T)	5 K
Cell size (H)	0.60 m

In the simulations, the non-dimensional control parameters for the particles include the density ratio of the particle to its surrounding fluid $\Gamma = \rho_p/\rho_f$, and the size ratio $\Xi = d_p/l_f$. By combing the Γ and Ξ, we can obtain the particle Stokes number (St) and the Archimedes number (Ar) as

$$St = \frac{\tau_p}{\tau_\eta} = \frac{\rho_p d_p^2/(18\mu_f)}{\sqrt{\nu/\langle\varepsilon_u\rangle_{V,t}}}, \qquad Ar = \sqrt{\frac{\rho_p - \rho_f}{\rho_f}\frac{g d_p^3}{\nu^2}} \tag{9}$$

where τ_p is particle response time. The St describes the particle inertia relative to that of the fluid, and the Ar describes the ratio of gravity forces to the viscous forces. Because we have fixed the Ra and the Pr in the simulation, namely thermal convection related quantities are fixed, we then have $St \propto \rho_p$, $Ar \propto \rho_p^{1/2}$ and $St \propto d_p^2$, $Ar \propto d_p^{3/2}$. The St and the Ar numbers can be uniquely determined by d_p and ρ_p, as shown in Fig. 2. We explore the parameter space of 10 μm $\leq d_p \leq$ 100 μm and 400 kg/m^3 $\leq \rho_p \leq$ 4000 kg/m^3, denoted by the black circles in Fig. 2. We note that the estimated Kolmogorov length scale is $\eta_K = 2.27$ mm, and the largest particle volume fraction of all cases is only 0.02%. Thus, for dilute particles with diameters fall in the range mentioned above, the one-way coupling strategy is justified to model their motions. For particles with larger number but still similar size, i.e., particles with higher particle volume fraction, a four-way coupling strategy is necessary to describe the interactions between the particle and its surrounding fluid[46,47].

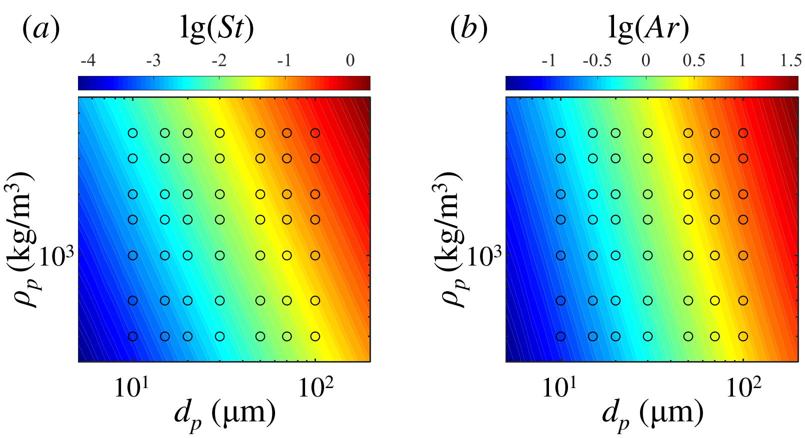

FIG. 2. (*a*) The logarithmic of the particle Stokes number and (*b*) the logarithmic of the Archimedes number as functions of the particle diameter d_p and particle density ρ_p. The black circles represent our simulation parameters.

III. RESULTS AND DISCUSSION

A. Particle transport in the convection cell

Figure 3 shows the snapshots of the instantaneous particles' positions for $d_p = 10$ μm and 400 kg/m^3 $\leq \rho_p \leq 4000$ kg/m^3 (corresponding to $3.67\times10^{-4} \leq St \leq 3.67\times10^{-3}$ and $0.115 \leq Ar \leq 0.366$) at $t = 500\ t_f$ (corresponding to $t \approx 951.6$ s). Here, we denote the time origin $t = 0$ as the instant when the particles are released in the turbulence. At such small St and Ar, the particles' motions are profoundly affected by the LSC of the convection. Specifically, these relatively small particles are well dispersed in the turbulence, and they can remain suspended for a long time. On the other hand, we also notice the differences in the spatial pattern of particles' positions: the particles are more homogeneously distributed in the turbulence at relatively smaller particle density (see Figs. 3(a-c), which corresponds to $3.67\times10^{-4} \leq St \leq 9.19\times10^{-4}$ and $0.115 \leq Ar \leq 0.183$). In contrast, they tend to cluster into bands at relatively larger particle density (see Figs. 3(d-f), which corresponds to $1.84\times10^{-3} \leq St \leq 3.67\times10^{-3}$ and $0.259 \leq Ar \leq 0.366$). The clustered particle are repelled from regions of high vorticity, as visualized by the contour of vorticity $\omega = \nabla\times\mathbf{u}$ in Figs. 3(*d-f*), which shows similar pattern (but at much smaller St) compared to those in homogeneous isotropic turbulence[14–17]. We also notice there are fewer particles in the corner rolls of the convection with the increase of particle density. The previous study by Park et al.[31] indicates that the clustering behavior in thermal turbulence occurs at much larger particle St number (namely $St \approx 1$) when the dimensionless particle settling velocity $V_g/U_{buoy} = \left[\rho_p d_p^2 g/(18\mu_f)\right]/\sqrt{g\beta\Delta H}$ is fixed as 0.001. However, if we assume the carrier fluid is air, a quantitative estimation shows that simultaneously achieving $St \approx 1$ and would result in artificially tiny gravity value (almost seven orders of magnitude smaller than 9.8 m/s^2).

The-above visualizations illustrate the preferential distribution of particles in the thermal turbulence. To quantitatively describes the spatial distribution of the particles, we divide the simulation domain into 100×100 uniform subcells and calculate the local particle number density as

$$n(i,j,t) = \frac{N(i,j,t)}{N_{\text{total}}(t)} \tag{10}$$

where $N(i,j,t)$ is the number of suspended particles found inside the (i,j)-th small square subcell (here $1 \leq i,j \leq 100$), and $N_{\text{total}}(t)$ is the number of suspended particle in the whole convection cell at time t. In Fig. 4, we plot the local particle number density at $t = 500\ t_f$, where we can observe homogenous local particle number densities for 400 kg/m^3 $\leq \rho_p \leq 1000$ kg/m^3. The local particle

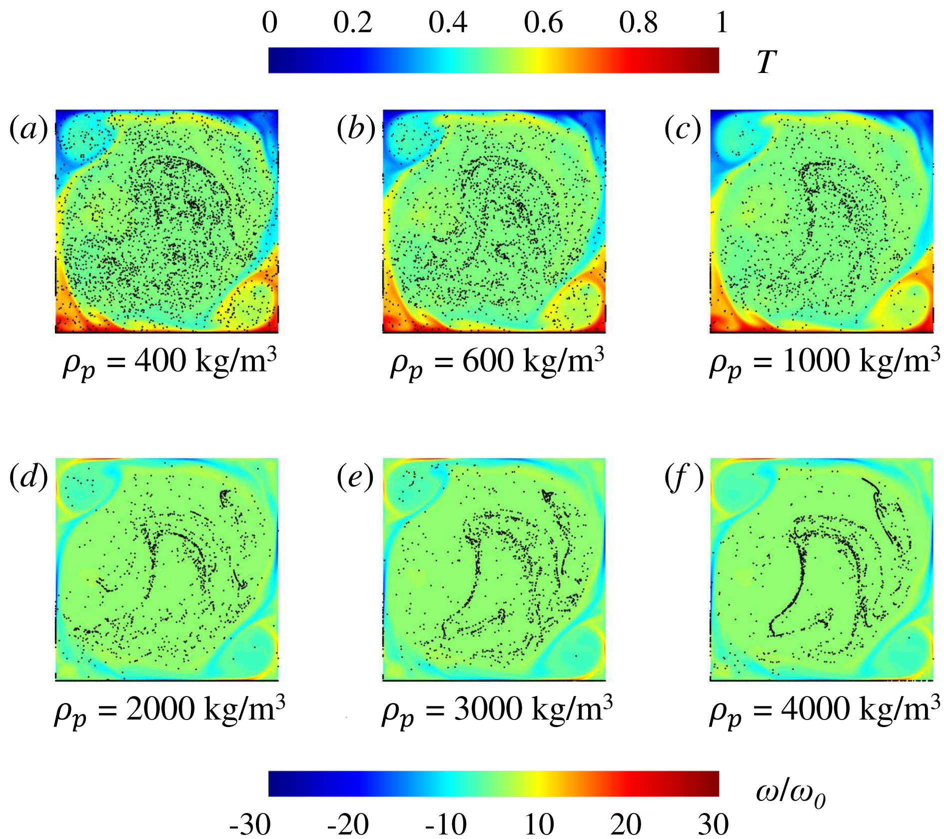

FIG. 3. Snapshots of the particles' positions at $t = 500\ t_f$. The top panel (*a*-*c*) shows the temperature field (contour), while the bottom panel (*d*-*f*) shows the vorticity field (contour). ω_0 denotes the instantaneous vorticity at the cell center. The diameters of these particles are 10 μm.

number densities are more inhomogeneous for 2000 kg/m$^3 \leq \rho_p \leq$ 4000 kg/m^3, which is due to higher particle inertia and longer particle response time to the carrier flow.

We further calculate the relative standard deviation of the local particle number density, namely, the root-mean-square (r.m.s.) of particle number density normalized by the volume-averaged particle number density, which is defined as

$$\text{relative std.} = \frac{1}{\bar{n}(t)}\sqrt{\frac{\sum_{i,j}\left[n(i,j,t) - \bar{n}(t)\right]^2}{100 \times 100}} \tag{11}$$

Here, $\bar{n}(t)$ denotes the volume-averaged particle number density at time t. In Fig. 5, we plot the time histories of the relative standard deviation for particles with a diameter of 10 μm. We can see that the deviations decrease rapidly during the initial transient state (i.e., $t \lesssim 250\ t_f$), which is due to the dispersion of the particle group after being released in the turbulence. At $t \gtrsim 250\ t_f$, the relative standard deviations nearly reach a plateau, indicating the well dispersion of the particles in

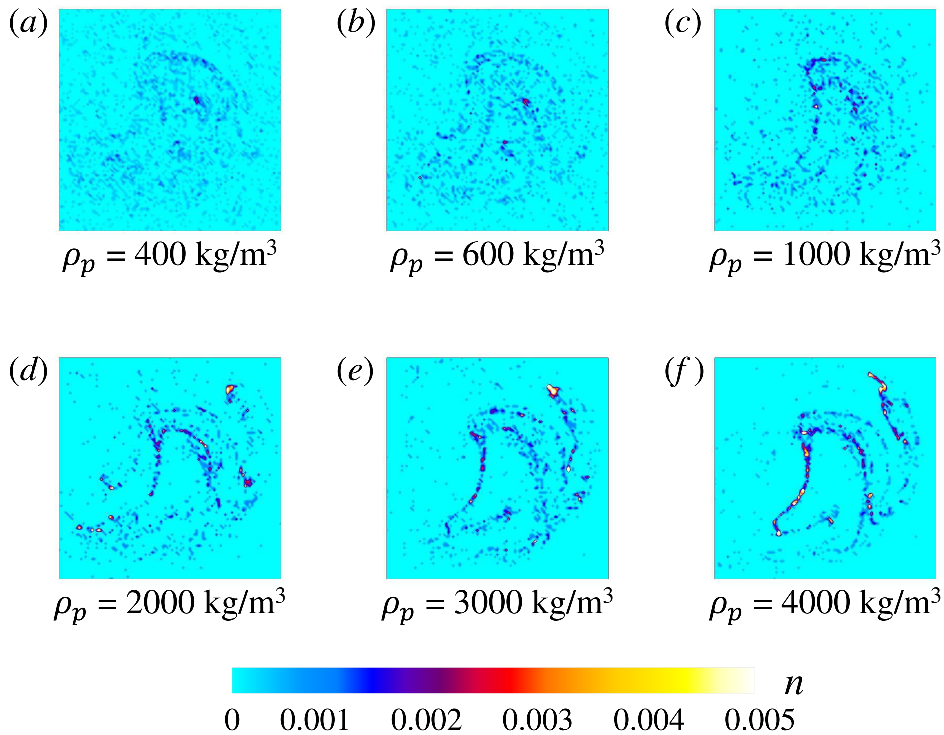

FIG. 4. Snapshots of the instantaneous local particle number density at $t = 500\ t_f$. The diameters of these particles are 10 μm, and their densities are (*a*) 400 kg/m^3, (*b*) 600 kg/m^3, (*c*) 1,000 kg/m^3, (*d*) 2,000 kg/m^3, (*e*) 3,000 kg/m^3, (*f*) 4,000 kg/m^3.

the turbulence. We also found that the relative standard deviation of local particle number density depends on the *St* and *Ar*, as light density and small size of the particles favor their dispersion.

We then analyze the statistics of particles' trajectories by calculating their mean-square displacement $\mathrm{MSD}(\tau) = \langle [\mathbf{r}(t+\tau) - \mathbf{r}(t)]^2 \rangle$. Here, $\mathbf{r}(t)$ is the particle's position at time t, and τ is the lag time between the two positions taken by the particles. The average $\langle \cdots \rangle$ represents a time-average over t and an ensemble-average over trajectories. When a particle is deposited on the wall, we will stop tracking its trajectory. Fig. 6(a) shows the MSD for particles with $d_p = 10$ μm and ρ_p = 1,000 kg/m^3, where we can see that the MSD exhibits a ballistic regime at short time intervals, namely, MSD $\propto \tau^2$ for $\tau \le t_f$. At longer time intervals, the MSD asymptotically approaches a plateau value, indicating confined motions for the particles, which is due to the walls of the convection cell. Previously, there were contrary results[48,49] on pair particle dispersion in different directions, because the turbulent thermal convection is anisotropic with vertically rising or falling plumes. Here, we further examine whether the group of particles dispersion properties

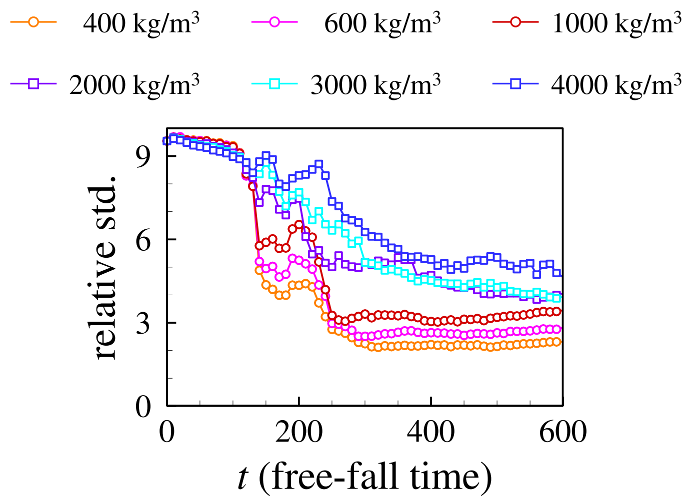

FIG. 5. Time histories of the relative standard deviation for local particle number density particles with $d_p = 10\ \mu$m.

are isotropic. We decompose the distance vector $\mathbf{r}$ into a lateral ($\mathbf{r}_x$) and vertical ($\mathbf{r}_y$) part, and calculate the MSD in the lateral and vertical directions separately as

$$\mathrm{MSD}_x(\tau) = \langle [\mathbf{r}_x(t+\tau) - \mathbf{r}_x(t)]^2 \rangle, \quad \mathrm{MSD}_y(\tau) = \langle [\mathbf{r}_y(t+\tau) - \mathbf{r}_y(t)]^2 \rangle \tag{12}$$

From Fig. 6(b), we can see that the MSD is isotropic at short time intervals, while the differences between MSD_x and MSD_y are apparent at longer time intervals. We can also roughly estimate how the particle is constrained in different directions by calculating the square root of the plateau MSD value. The results in Fig. 6(b) indicates that the vertical region of constraint is a bit larger than that of the lateral region. The reason is that most of the suspended particles are trapped within the elliptical primary roll, whose major axis has a longer vertical component than the horizontal one. Thus, when the LSC advects the particles, they will 'travel' longer distance in the vertical direction than the lateral one.

The-above analysis focused on relatively small particles that will be dispersed in the turbulence. In contrast, for relatively large particles (e.g., particles with $d_p = 100\ \mu$m), they will sediment quickly after being released in the turbulence, as shown in Fig. 7. The carrier flow minorly influences the particles' motions, and the particle group almost remains their initial shape (namely the square shape due to the artificial simulation setting, see Fig. 1) during the sedimentation. Because the LSC of the convection is clockwise rotated, the deposition location of the particle group on the bottom wall will be left side offset their initial horizontal position. We also observe that the shape of the lighter particle group will stretch more during the sedimentation. In comparison, heavier

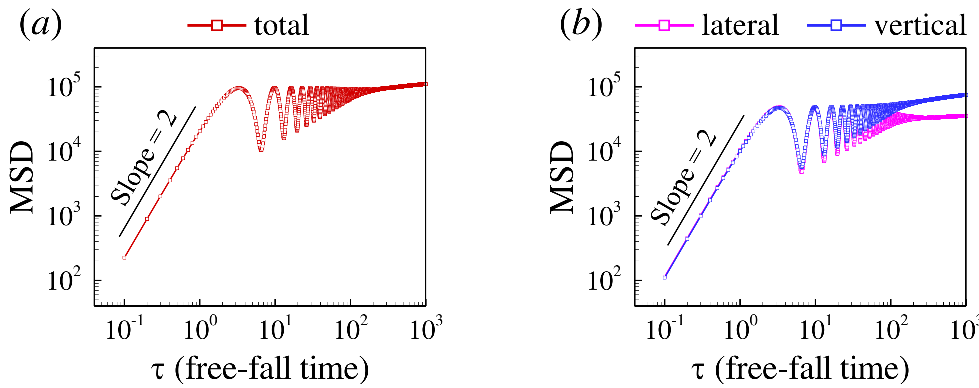

FIG. 6. (*a*) The total mean-square displacement (MSD) of particles' trajectories, (*b*) the MSD in the lateral and vertical directions for particles with d_p = 10 μm and ρ_p = 1,000 kg/m^3.

particle group sediments faster and has shorter horizontal offset distance for final deposition.

B. Particle deposition on the wall

We measure the particle deposition ratio as the number of deposited particles on the walls over the number of total released particles in the turbulence. In Figs. 8(a) and (b), we plot time histories of the deposition ratio for particles with d_p = 10 μm and 30 μm, respectively. Here, we count the number of deposited particles on the four walls of the convection cell separately, as well as their summations. We found that most of the particles are deposited on the bottom wall, while there is no particle deposited on the top wall. In addition, we observe a tiny portion of the particles are deposited on the left and right walls. An interesting observation is that there are more particles deposited on the left vertical wall compared to that on the right vertical wall. Because the LSC of the convection is clockwise rotated, the horizontal wind (from right to left) in the lower part of the convection cell will drive the particles from the right side of the cell to the left side. When the rising hot plumes along the left vertical wall are not able to lift the particles, they will deposit on the left wall. A similar preferential deposition pattern on hot vertical walls was also found in the side-heated convection cell[29]. To further verify the above conjecture, we measure the particle deposition ratio in a tilted convection cell, where the rotation direction of the LSC is reversed compared to that in the leveled cell. Figs. 8(c) and (d) show the particle deposition ratio in the tilted cell with vertical axis counter-clockwise rotates a small angle of 0.1°, such that only the LSC rotation direction is reversed. Still, other flows and heat transfer properties are almost not

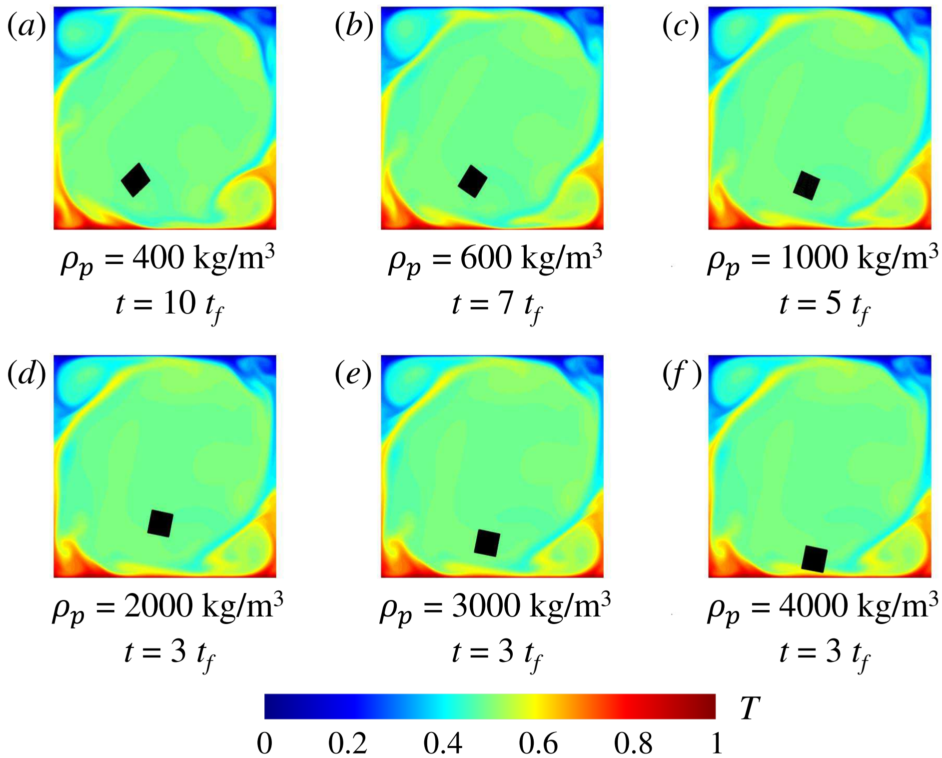

FIG. 7. Snapshots of the instantaneous temperature field and particles' positions (*a*) for ρ_p = 400 kg/m^3 at $t = 10\ t_f$, (*b*) for ρ_p = 600 kg/m^3 at $t = 7\ t_f$, (*c*) for ρ_p = 1,000 kg/m^3 at $t = 5\ t_f$, (*d*) for $\rho_p = 2{,}000$ kg/m^3 at $t = 3\ t_f$, (*e*) for $\rho_p = 3{,}000$ kg/m^3 at $t = 3\ t_f$, (*f*) for $\rho_p = 4{,}000$ kg/m^3 at $t = 3\ t_f$. The diameters of these particles are 100 μm.

influenced with such small tilted angle[50,51]. In the tilted case, the hot plumes arise along the right vertical wall, and we can see more particles are deposited on the right vertical wall. Thus, a general conclusion is that particles prefer to deposited on the vertical wall where the hot plumes arise.

With the numerical simulations in a wide range of d_p and ρ_p parameter spaces, we can then obtain the phase diagram for the particle deposition positions on the walls. As shown in Fig. 9, particles with smaller d_p and ρ_p are more easily suspended and well dispersed in the flow; thus, the particles have chances to deposit on the left and right vertical walls, and of course, most of the particles will deposit on the bottom wall due to the gravity sedimentation (denoted as 'Three walls' in the phase diagram). For particles with larger d_p and ρ_p, the carrier flows minorly influences them, and the particles will only deposit on the bottom wall (denoted as 'One wall' in the phase diagram). The 'One wall' deposition state also corresponds to the initially released particle group not well dispersed in the turbulence. Sandwiched between the 'Three walls' and 'One wall' states

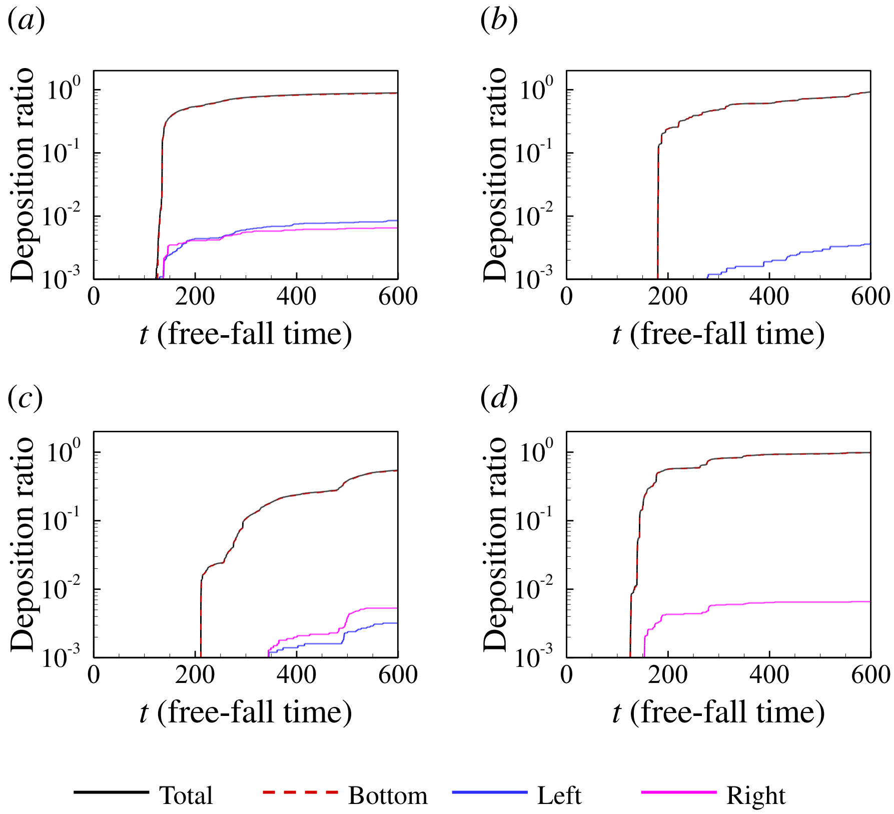

FIG. 8. Time histories of particle deposition ratio for particles with ρ_p = 1,000 kg/m^3, (*a*, *c*) d_p = 10 μm, (*b*, *d*) d_p = 30 μm. The convection cell is leveled in (*a*-*b*), while the cell counter-clockwise rotates 0.1° in (*c*-*d*).

is the ’Two walls’ state, where particles will deposit on the bottom wall and one vertical wall at medium d_p and ρ_p (namely, medium St and Ar). This transition state of particle deposition on only one vertical one is due to that particles exhibit cluster behavior and they are not well dispersed in the flow compared to the cases in ’Three walls’ state. On the other hand, in the transition state, the particles will still be majorly advected in the convection compared to the cases in ’One wall’ state, and if particles deposit, they will only deposit on vertical walls where the hot plumes arise. For the explored parameter space of d_p and ρ_p, we confirm that there are no particles deposited on the top wall. From the phase diagram, we can also observe the borders between different states are strongly correlated with the St and the Ar numbers.

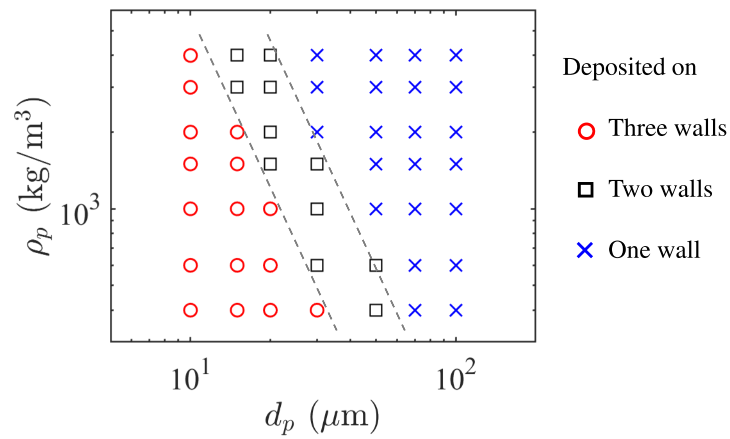

FIG. 9. Phase diagram of the particle deposition positions on the wall. The gray dashed lines represent the rough borders between different states.

IV. CONCLUSIONS

In this work, we have performed numerical simulations of particle motion in turbulent thermal convection. Specifically, we analyzed the statistics of particle transport and deposition in 2D square RB convection cell. The main findings are summarized as follows:

1. The suspended particles are more homogeneously distributed in the turbulence at *St* less than 10^{-3}, and they tend to cluster into bands for $10^{-3} \lesssim St \lesssim 10^{-2}$. At even larger *St*, the particles' motion will be minorly influenced by the turbulence, and they will sediment quickly and deposit on the boundary walls.

2. At short time intervals, the MSD exhibits a ballistic regime, and it is isotropic in vertical and lateral directions. At longer time intervals, the MSD asymptotically approaches a plateau value, indicating confined motions for the particles. The anisotropic of MSD at longer times intervals is attributed to the tilted elliptical primary roll, in which most of the particles are trapped and being advected.

3. We obtained a phase diagram of the particle deposition positions, and three deposition states were identified: particles deposited on three walls, two walls, and one wall. Although most of the particles will deposit on the bottom wall, we found there is still a tiny portion of particles deposited on the vertical wall. Moreover, the particles preferred to deposit on the vertical wall where the hot plumes arise.

ACKNOWLEDGMENTS

This work was supported by the National Natural Science Foundation of China (NSFC) through Grant Nos. 11902268 and 51906044, the Fundamental Research Funds for the Central Universities of China (No. D5000200570) and the 111 project of China (No. B17037). The simulations were carried out at LvLiang Cloud Computing Center of China, and the calculations were performed on TianHe-2.

DATA AVAILABILITY STATEMENT

The data that support the findings of this study are available from the corresponding author upon reasonable request.

REFERENCES

[1] A. Guha, "Transport and deposition of particles in turbulent and laminar flow," Annual Review of Fluid Mechanics **40**, 311–341 (2008).

[2] F. Toschi and E. Bodenschatz, "Lagrangian properties of particles in turbulence," Annual Review of Fluid Mechanics **41**, 375–404 (2009).

[3] S. Tenneti and S. Subramaniam, "Particle-resolved direct numerical simulation for gas-solid flow model development," Annual Review of Fluid Mechanics **46**, 199–230 (2014).

[4] V. Mathai, D. Lohse, and C. Sun, "Bubbly and buoyant particle–laden turbulent flows," Annual Review of Condensed Matter Physics **11**, 529–559 (2020).

[5] J. H. Seinfeld and S. N. Pandis, *Atmospheric chemistry and physics: from air pollution to climate change* (John Wiley & Sons, 2016).

[6] D. Norbäck, C. Lu, Y. Zhang, B. Li, Z. Zhao, C. Huang, X. Zhang, H. Qian, Y. Sun, J. Wang, *et al.*, "Sources of indoor particulate matter (PM) and outdoor air pollution in China in relation to asthma, wheeze, rhinitis and eczema among pre-school children: Synergistic effects between antibiotics use and PM10 and second hand smoke," Environment International **125**, 252–260 (2019).

[7] L. Bourouiba, E. Dehandschoewercker, and J. W. Bush, "Violent expiratory events: on coughing and sneezing," Journal of Fluid Mechanics **745**, 537–563 (2014).

[8]R. Mittal, R. Ni, and J.-H. Seo, "The flow physics of COVID-19," Journal of Fluid Mechanics **894**, F2 (2020).

[9]T. Dbouk and D. Drikakis, "On coughing and airborne droplet transmission to humans," Physics of Fluids **32**, 053310 (2020).

[10]S. Chaudhuri, S. Basu, P. Kabi, V. R. Unni, and A. Saha, "Modeling the role of respiratory droplets in Covid-19 type pandemics," Physics of Fluids **32**, 063309 (2020).

[11]S. Balachandar and J. K. Eaton, "Turbulent dispersed multiphase flow," Annual Review of Fluid Mechanics **42**, 111–133 (2010).

[12]M. A. van der Hoef, M. van Sint Annaland, N. Deen, and J. Kuipers, "Numerical simulation of dense gas-solid fluidized beds: a multiscale modeling strategy," Annual Review of Fluid Mechanics **40**, 47–70 (2008).

[13]M. Maxey, "Simulation methods for particulate flows and concentrated suspensions," Annual Review of Fluid Mechanics **49**, 171–193 (2017).

[14]L.-P. Wang and M. R. Maxey, "Settling velocity and concentration distribution of heavy particles in homogeneous isotropic turbulence," Journal of Fluid Mechanics **256**, 27–68 (1993).

[15]T. Bosse, L. Kleiser, and E. Meiburg, "Small particles in homogeneous turbulence: Settling velocity enhancement by two-way coupling," Physics of Fluids **18**, 027102 (2006).

[16]E. Calzavarini, M. Kerscher, D. Lohse, and F. Toschi, "Dimensionality and morphology of particle and bubble clusters in turbulent flow," Journal of Fluid Mechanics **607**, 13–24 (2008).

[17]Q. Zhang, H. Liu, Z. Ma, and Z. Xiao, "Preferential concentration of heavy particles in compressible isotropic turbulence," Physics of Fluids **28**, 055104 (2016).

[18]G. Ahlers, S. Grossmann, and D. Lohse, "Heat transfer and large scale dynamics in turbulent Rayleigh-Bénard convection," Reviews of Modern Physics **81**, 503 (2009).

[19]D. Lohse and K.-Q. Xia, "Small-scale properties of turbulent Rayleigh-Bénard convection," Annual Review of Fluid Mechanics **42**, 335–364 (2010).

[20]F. Chillà and J. Schumacher, "New perspectives in turbulent Rayleigh-Bénard convection," The European Physical Journal E **35**, 58 (2012).

[21]K.-Q. Xia, "Current trends and future directions in turbulent thermal convection," Theoretical and Applied Mechanics Letters **3**, 052001 (2013).

[22]A. Mazzino, "Two-dimensional turbulent convection," Physics of Fluids **29**, 111102 (2017).

[23]B.-F. Wang, Q. Zhou, and C. Sun, "Vibration-induced boundary-layer destabilization achieves massive heat-transport enhancement," Science Advances **6**, eaaz8239 (2020).

[24] M. K. Verma, *Physics of buoyant flows: from instabilities to turbulence* (World Scientific, 2018).
[25] T. Hiroaki and M. Hiroshi, "Turbulent natural convection in a horizontal water layer heated from below," International Journal of Heat and Mass Transfer **23**, 1273–1281 (1980).
[26] R. Krishnamurti and L. N. Howard, "Large-scale flow generation in turbulent convection," Proceedings of the National Academy of Sciences **78**, 1981–1985 (1981).
[27] Q. Zhou, C. Sun, and K.-Q. Xia, "Morphological evolution of thermal plumes in turbulent Rayleigh-Bénard convection," Physical Review Letters **98**, 074501 (2007).
[28] H.-D. Xi, S. Lam, and K.-Q. Xia, "From laminar plumes to organized flows: the onset of large-scale circulation in turbulent thermal convection," Journal of Fluid Mechanics **503**, 47–56 (2004).
[29] R. Puragliesi, A. Dehbi, E. Leriche, A. Soldati, and M. Deville, "DNS of buoyancy-driven flows and Lagrangian particle tracking in a square cavity at high Rayleigh numbers," International Journal of Heat and Fluid Flow **32**, 915–931 (2011).
[30] M. Lappa, "On the transport, segregation, and dispersion of heavy and light particles interacting with rising thermal plumes," Physics of Fluids **30**, 033302 (2018).
[31] H. J. Park, K. O'Keefe, and D. H. Richter, "Rayleigh-Bénard turbulence modified by two-way coupled inertial, nonisothermal particles," Physical Review Fluids **3**, 034307 (2018).
[32] S. Chen and G. D. Doolen, "Lattice Boltzmann method for fluid flows," Annual Review of Fluid Mechanics **30**, 329–364 (1998).
[33] C. K. Aidun and J. R. Clausen, "Lattice-Boltzmann method for complex flows," Annual Review of Fluid Mechanics **42**, 439–472 (2010).
[34] A. Xu, W. Shyy, and T. Zhao, "Lattice Boltzmann modeling of transport phenomena in fuel cells and flow batteries," Acta Mechanica Sinica **33**, 555–574 (2017).
[35] H. Huang, M. Sukop, and X. Lu, *Multiphase lattice Boltzmann methods: Theory and application* (John Wiley & Sons, 2015).
[36] A. Xu, L. Shi, and T. Zhao, "Accelerated lattice Boltzmann simulation using GPU and OpenACC with data management," International Journal of Heat and Mass Transfer **109**, 577–588 (2017).
[37] A. Xu, L. Shi, and T. Zhao, "Thermal effects on the sedimentation behavior of elliptical particles," International Journal of Heat and Mass Transfer **126**, 753–764 (2018).
[38] A. Xu, L. Shi, and H.-D. Xi, "Lattice Boltzmann simulations of three-dimensional thermal convective flows at high Rayleigh number,"

International Journal of Heat and Mass Transfer **140**, 359–370 (2019).

[39] A. Xu, L. Shi, and H.-D. Xi, "Statistics of temperature and thermal energy dissipation rate in low-Prandtl number turbulent thermal convection," Physics of Fluids **31**, 125101 (2019).

[40] G. A. Voth and A. Soldati, "Anisotropic particles in turbulence," Annual Review of Fluid Mechanics **49**, 249–276 (2017).

[41] E. Calzavarini, L. Jiang, and C. Sun, "Anisotropic particles in two-dimensional convective turbulence," Physics of Fluids **32**, 023305 (2020).

[42] R. Clift, J. Grace, and M. Weber, *Bubbles, drops, and particles* (Academic Press, 1978).

[43] J. Duguid, "The size and the duration of air-carriage of respiratory droplets and droplet-nuclei," The Journal of Hygiene **44**, 471–479 (1946).

[44] B. I. Shraiman and E. D. Siggia, "Heat transport in high-Rayleigh-number convection," Physical Review A **42**, 3650 (1990).

[45] Y. Zhang, Q. Zhou, and C. Sun, "Statistics of kinetic and thermal energy dissipation rates in two-dimensional turbulent Rayleigh–Bénard convection," Journal of Fluid Mechanics **814**, 165–184 (2017).

[46] G. Akiki, T. Jackson, and S. Balachandar, "Pairwise interaction extended point-particle model for a random array of monodisperse spheres," Journal of Fluid Mechanics **813**, 882–928 (2017).

[47] G. Akiki, W. Moore, and S. Balachandar, "Pairwise-interaction extended point-particle model for particle-laden flows," Journal of Computational Physics **351**, 329–357 (2017).

[48] J. Schumacher, "Lagrangian dispersion and heat transport in convective turbulence," Physical Review Letters **100**, 134502 (2008).

[49] R. Ni and K.-Q. Xia, "Experimental investigation of pair dispersion with small initial separation in convective turbulent flows," Physical Review E **87**, 063006 (2013).

[50] C. Sun, H.-D. Xi, and K.-Q. Xia, "Azimuthal symmetry, flow dynamics, and heat transport in turbulent thermal convection in a cylinder with an aspect ratio of 0.5," Physical Review Letters **95**, 074502 (2005).

[51] Q. Wang, S.-N. Xia, B.-F. Wang, D.-J. Sun, Q. Zhou, and Z.-H. Wan, "Flow reversals in two-dimensional thermal convection in tilted cells," Journal of Fluid Mechanics **849**, 355–372 (2018).